Quantitatively Probing the Al Distribution in Zeolites

Aleksei Vjunov,[†] John L. Fulton,*[,†] Thomas Huthwelker,[‡] Sonia Pin,[‡] Donghai Mei,[†] Gregory K. Schenter,[†] Niranjan Govind,[§] Donald M. Camaioni,[†] Jian Zhi Hu,[†] and Johannes A. Lercher*[,†,⊥]

[†]Institute for Integrated Catalysis, [§]Environmental Molecular Sciences Laboratory, Pacific Northwest National Laboratory, P.O. Box 999, Richland, Washington 99352, United States

[‡]Swiss Light Source, Laboratory for Catalysis and Sustainable Chemistry (LSK), Paul Scherrer Institut (PSI), 5232 Villigen, Switzerland

[⊥]Department of Chemistry and Catalysis Research Institute, TU München, Lichtenbergstrasse 4, 85748 Garching Germany

S *Supporting Information*

ABSTRACT: The degree of substitution of Si^{4+} by Al^{3+} in the oxygen-terminated tetrahedra (Al T-sites) of zeolites determines the concentration of ion-exchange and Brønsted acid sites. Because the location of the tetrahedra and the associated subtle variations in bond angles influence the acid strength, quantitative information about Al T-sites in the framework is critical to rationalize catalytic properties and to design new catalysts. A quantitative analysis is reported that uses a combination of extended X-ray absorption fine structure (EXAFS) analysis and ^{27}Al MAS NMR spectroscopy

supported by DFT-based molecular dynamics simulations. To discriminate individual Al atoms, sets of ab initio EXAFS spectra for various T-sites are generated from DFT-based molecular dynamics simulations, allowing quantitative treatment of the EXAFS single- and multiple-photoelectron scattering processes out to 3−4 atom shells surrounding the Al absorption center. It is observed that identical zeolite types show dramatically different Al distributions. A preference of Al for T-sites that are part of one or more 4-member rings in the framework over those T-sites that are part of only 5- and 6-member rings in an HBEA150 zeolite has been determined using this analysis.
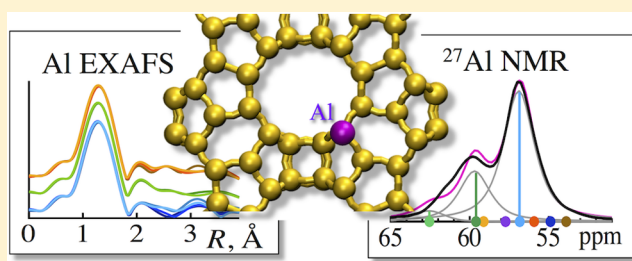
■ INTRODUCTION

Zeolites are widely used as sorbents and catalysts because their well-defined pore structure and adjustable acidity lead to high activity for a large variety of reactions.[1,2] The exceptional catalytic properties[3] are attributed to the combination of steric constraints and the specific properties of the active site, in particular the Brønsted acid strength and concentration, which is associated with the substitution of Al in the zeolite framework.[4,5]

It has been inferred from kinetic measurements that for a given zeolite framework, the specific substitution of Al atoms dramatically affects the catalytic activity.[6] It has also been proposed that the stability of zeolites with regard to dealumination as well as acid strength distribution depends upon the position of the Al T-sites in the zeolite structure.[7] Thus, information about the location and stability of the Al T-sites in the zeolite framework is essential to understand the activity and availability of specific sites for catalysis. Such information also provides the basis to design new and improve existing zeolites with respect to activity and selectivity.

The location of Al in the zeolite lattice impacts the environment of the acid site, offering varying steric access for reacting molecules as well as subtle differences in acid strength due to variations in the bond angles of the tetrahedra.[8,9] More

acute Al−O−Si bond angles have been postulated to induce higher acid strength.[10] An empirical relation between the Al−O−Si bond angle and the ^{27}Al NMR chemical shifts is frequently suggested as a means to locate Al in a zeolite lattice.[11,12]

^{27}Al magic angle spinning (MAS) NMR has been extensively applied to study Al T-sites in zeolites for differentiating tetrahedrally and octahedrally coordinated Al^{3+} at framework and extra-framework positions.[13] The analysis of the Al T-site distribution, however, remains a difficult task, especially for zeolites with a high number of crystallographically distinct framework positions.[14] The spectral resolution of the tetrahedral Al sites also suffers from line broadening[15] due to the quadrupolar character of Al.[16] This limitation has been partly overcome by quantitatively predicting ^{27}Al NMR chemical shifts using DFT[17,18] and hybrid approaches between quantum and molecular mechanics.[19,20] In this way, parameters such as Al dilution level and the presence of silanol defect sites in the sample framework can be included to further improve accuracy of the analysis.[21] Although it is internally consistent,

this approach has never been confirmed by an independent method.

An accurate method to determine the T-site distribution has been conceptually shown for relatively simple aluminosilicates using the X-ray standing wave (XSW) technique. van Bokhoven et al.[22] applied this XSW method to the analysis of a macroscopic single crystal of scolecite to show that all Al is selectively present in one of only two different Al T-sites.

Because X-ray absorption spectroscopy is conceptually sensitive to the local structure around zeolite T-sites, we have taken a bold approach using extended X-ray absorption spectroscopy (EXAFS) to evaluate the longer-range interatomic distances around Al T-sites, which are related to the local environment. In addition, we also use the more traditional analysis of the region close to the absorption edge (XANES; X-ray absorption near edge spectroscopy) to derive information about the symmetry of the Al T-sites.[23,24] We emphasize at this point that EXAFS analysis has the potential to accurately determine the nearby Al–O and Al–Si distances and their angular correlations up to a distance of ~3−4 atom shells beyond the central Al T-sites. This potential, however, has not been used for quantitative analysis of zeolites (other than for evaluating the first-shell Al−O bond lengths),[25,26] because of the many factors limiting the data quality during acquisition of EXAFS spectra at low X-ray energies (1559 eV, Al K-edge), including achieving constant high X-ray flux at the sample; stable beam position; harmonic-free beam; stable sample detectors; and finally, properly accounting for the strong X-ray absorption by the sample in that energy region. The combination of a very high flux undulator source, an improved X-ray monochromator, and an improved detector has allowed[27] the acquisition of high-quality spectra sufficient for a quantitative treatment of the higher-order scattering paths required to determine the zeolite structure.

Even with this progress, quantitative evaluation of EXAFS remains challenging. The standard EXAFS analysis protocol involves selecting the most probable set of photoelectron scattering paths and then fitting their atom distances, disorder (Debye−Waller factors or DWF), and coordination numbers (CN). This standard approach becomes intractable when considering that the multiple Al T-site occupancies lead to large numbers of fitted parameters, which exceed the information content of the experimentally measured spectra. To circumvent this constraint, the structural parameters (bond distance, DWF, and CN's) for each T-site were quantitatively determined from first-principles calculations using ab initio molecular dynamics simulation. These calculated dynamical representations of the Al T-site structure then provide the input for calculating the molecular dynamics-EXAFS (MD-EXAFS) spectrum.[28] This represents an ab initio procedure for calculating the photoelectron single- and multiple-scattering pathways (~10^7 in one trajectory) out to about 6 Å without the need for any adjustable parameters. As a note in passing, we would like to emphasize the generality of this approach, which provides a new opportunity for the evaluation of impurity locations in doped semiconductors[29] or ferromagnetic films.[30]

In the present case, MD-EXAFS is used to analyze Al siting in a large-pore zeolite, Beta, which is central to many fine chemical reactions and petrochemical transformations.[31−34] Figure 1 provides a representation along the [010] axis for the HBEA zeolite showing the primary catalytic channels represented as 6−7 Å diameter straight pores defined by the 12-member rings. The [100] axis has a nearly identical structure
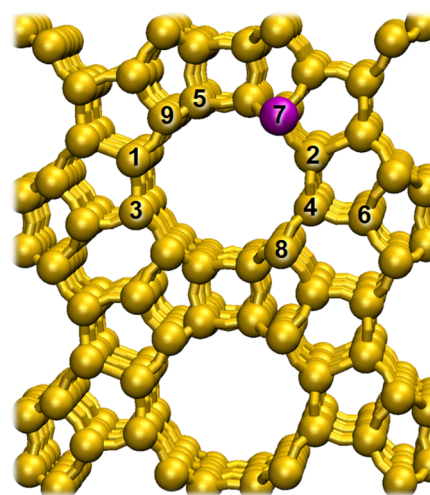

Figure 1. Representation of HBEA zeolite framework in the [010] axis with one of the nine different T-sites substituted by an Al^{3+} ion (purple). Oxygens and the proton are not shown to emphasize ring structures containing 4, 5, 6, and 12 silicon atoms.

that is likewise populated with a set of parallel, nonintersecting 6−7 Å pores. On the other hand, the [001] axis has slightly smaller 5−6 Å pores, which also form 12-member rings, that zigzag to alternately intersect the primary pores along both the [100] and the [010] axes. The structure contains 4-, 5-, and 6-member rings forming the overall lattice with nine crystallographically different T-sites.

■ EXPERIMENT AND THEORY SECTION

Sample Description. HBEA25 (Si/Al = 12.5) and HBEA150 (Si/Al = 75), which was dealuminated via leaching, were received from Süd Chemie AG (Clariant), and HMOR (Si/Al = 45) was from Zeolyst, all in hydrogen form. The samples were washed with deionized water, dried in vacuum at ambient temperature, and then stored for more than 2 weeks under ambient temperature and humidity prior to measurement. $Na_2Al_2O_4$ (99.95% anhydrous) (tetrahedral-Al), $AlCl_3$ (99.999% anhydrous), and α-Al_2O_3 (99%) (octahedral-Al) were obtained from Sigma-Aldrich and were used without further processing.

The HBEA150 and HBEA25 samples used in this work are mixtures of the two polymorphic forms A and B.[35] From inspection of XRD spectra,[36,37] the two polymorphs are present in a 50/50 ratio (see SI for more detail). Because both polymorphs A and B are constructed from identical centrosymmetric tertiary building units,[38,39] the local geometry is nearly identical for the two polymorph structures, and thus, the presence of both polymorphs does not affect the EXAFS and NMR analysis in this work. The similarity of the T-site structures in the two polymorphs has been demonstrated in NMR and pair-distribution-function analyses.[40−42] Additional details on the zeolite Beta polymorphs and their structural similarity are provided in the Supporting Information (SI).

Al K-Edge EXAFS Experimental Methods. The Al K-edge EXAFS measurements were conducted at the Phoenix I, elliptical undulator beamline at the Swiss Light Source (SLS) at the Paul Scherrer Institute. Energy calibration was achieved by setting the inflection point of an Al foil spectrum to 1559.6 eV. The double-crystal monochromator employed a set of $KTiOPO_4$ (011) crystals to provide an energy resolution of

about 0.6 eV over a scan range for the Al K-edge from 1500 to 2100 eV, just below the P K-edge. Two Ni-coated mirrors were set at an angle of 1.45° to provide cutoff of higher harmonics. An unfocused 1.0 × 1.0 mm beam having a flux of ~10^9 photons/s was used. The sample chamber pressure was maintained at ~2.5×10^{-4} mbar. Measurements were typically performed in fluorescence mode, although several transmission measurements for individual samples were obtained to ascertain the magnitude of the self-absorption corrections. I_0 was measured as total electron yield signal taken from a 0.5 μm thin polyester foil, which was coated with 50 nm of Ni. This I_0 detector was held in a miniaturized vacuum chamber (2.9 × 10^{-6} mbar), which was separated by a thin Kapton foil from the measurement chamber itself. The X-ray fluorescence was detected using a 4-element Vortex Si-drift diode detector. For transmission measurement, a Si diode was used.

ATHENA[43] software was used to remove the $\chi(k)$ oscillations from the background and, in certain instances, to apply (standard routines for) self-absorption correction of the XANES and EXAFS spectra of the concentrated standard compounds. The linear combination fitting tools within ATHENA were used to evaluate the Al T-site distributions based on MD-EXAFS $\chi(k)$ spectra. Two different reference compounds, α-Al_2O_3 and $Na_2Al_2O_4$, were also evaluated using the ARTEMIS[43] software package. Theoretical standards for these compounds were derived from FEFF9.[43]

During the background processing used to extract the $\chi(k)$ data from the background function, a Fourier filter cutoff distance, R_{bkg}, of 1.0 Å was used. We found that the atomic background function, $\mu_0(E)$, contains a strong multielectron absorption edge at $k = 5.3$ Å^{-1} due to the KL$_{II,III}$ transition.[44] This transition is strong for octahedral, and weak for tetrahedral O-coordination symmetry about the Al T-site. The EXAFS data were weighted by k^2 and truncated using a Hanning window with dk = 1.0 Å^{-1} in the range of 1.5 < k < 8.0 Å^{-1}. We estimated the value of the core hole factor, $S_0^2 = 1.0$, from fits to the two crystalline standards. The S_0^2 factor typically had an error of ~15%.

^{27}Al MAS NMR. The ultrahigh field ^{27}Al MAS NMR experiments were performed on a Varian-Agilent Inova 63 mm wide-bore 900 MHz NMR spectrometer. The main magnetic field was 21.1 T, and the corresponding ^{27}Al Larmor frequency was 234.56 MHz. Experiments were performed using a commercial 3.2 mm pencil type MAS probe. In a typical experiment, about 15 mg of sample powder was loaded into the rotor and measured at ambient temperature. The HBEA samples were stored under ambient humidity, leading to a hydrated surface that is expected to contain Al tetrahedra that have minimal distortions and that have the maximum ^{27}Al MAS NMR spectral resolution.[45] A single pulse sequence with a pulse length of 2.0 μs, corresponding to a pulse angle of 45°, was selected for acquiring each ^{27}Al MAS NMR spectrum with a recycle time of 1 s and total accumulation of 5000 scans. The spectra were acquired at a sample spinning rate of 20 kHz ± 2 Hz and were referenced to 1.5 M Al$(NO_3)_3$ in H_2O (0 ppm) using the center of the octahedral peak of solid γ-Al_2O_3 (at 13.8 ppm) as a secondary reference. The measurement uncertainty is estimated to be ±0.1 ppm.

For quantitative measurements, the weights of samples loaded into the MAS rotor were recorded, and four spectra were acquired to check the stability of the spectrometer. The matching and tuning conditions of the RF circuit of the NMR probe were set using a network analyzer. All other experimental

conditions were kept identical for all analyzed samples. In this way, the absolute peak areas normalized to the spectrometer standard were proportional to the Al in the sample. The spectra were analyzed using the MestreNova 8.1 software package.

DFT, Molecular Dynamics (MD) Simulations. The CP2K program package[46] was used to perform periodic DFT structure optimizations and MD simulations. To obtain structures of the different Al T-sites in HBEA (see Figure 2),
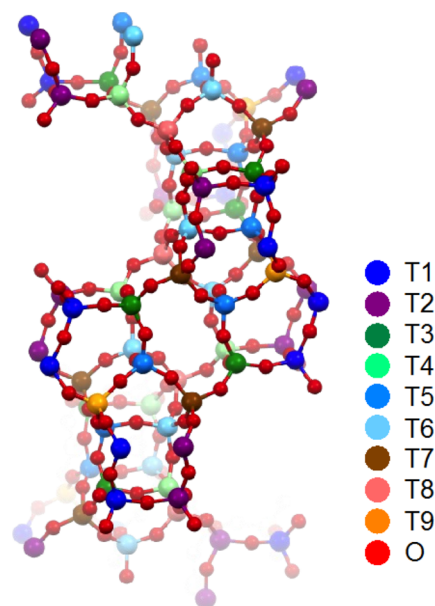

Figure 2. $[Si_{63}O_{128}Al_1]^{-1}$ structure showing the locations of the nine different T-sites.

a single unit cell of the BEA crystal[47] was modified by substituting an Al for a single Si atom to form a negatively charged $[Si_{63}O_{128}Al_1]^-$ cell. Although the presence of Al pairs (Al−O−Si−O−Al) was reported to affect the accuracy of Al chemical shift calculations,[48] such pairs were shown to be absent by ^{29}Si NMR, justifying the selected unit cell model (see the Supporting Information for details). For the acid form of the structure, a proton was placed on one of the O atoms neighboring the Al T-site to compensate the negative charge. The structures were optimized using the periodic DFT method with a mixed Gaussian and plane wave basis set. Core electrons were represented with norm-conserving Goedecker−Teter−Hutter pseudopotentials,[49] and the valence electron wave function was expanded in a double-ζ basis set with polarization functions[50] along with an auxiliary plane wave basis set with an energy cutoff of 360 eV. The generalized gradient approximation exchange-correlation functional of Perdew, Burke, and Enzerhof[51] was used for all calculations. Structure optimizations used the Broyden−Fletcher−Goldfarb−Shanno algorithm with SCF convergence criteria of 1.0×10^{-8} au. This process was repeated for each of the nine different T-sites labeled in Figure 2. The experimental lattice parameters (12.6614 × 12.6614 × 26.4061 Å^3) were used.[52]

MD-EXAFS. MD-EXAFS was used to simulate the EXAFS spectra of the Al T-sites. Initially, the nine different DFT optimized $[Si_{63}O_{128}Al_1]^-$ crystal structures were used to calculate a full set of EXAFS spectra from the ab initio scattering theory (FEFF9) by applying approximate global disorder parameters, σ^2, corresponding to 300 K (see SI Figure 7S). Using this initial screening method, the nine T-sites were

grouped into three sets, each set or group giving rise to uniquely different features in the predicted EXAFS (see SI Figure 7S). The sets were assigned as follows: Set A (T1, T2, T5, T6), Set B (T3, T4), and Set C (T7, T8, T9). The Al T-sites within each of these sets were found to have nearly identical EXAFS spectra.

On the basis of this assignment, the full MD trajectories at 300 K were calculated for three representative T-sites: T1, T3, and T7, corresponding to sets A, B, and C, respectively. For each MD calculation, the system was equilibrated at a constant temperature of 300 K for 10 ps with a Nosé−Hoover chain thermostat in the canonical ensemble.[53] These MD trajectories were then used to generate the MD-EXAFS spectra. The MD-EXAFS method has been described in detail previously.[54] Briefly, for each of the 10^4 snapshots from the MD trajectory, a set of atom positions was used to calculate a full set of scattering (single and multiple scattering) paths for all atoms within 6 Å of the Al T-site. This step generated 10^3 scattering paths for each snapshot of the trajectory. This process was repeated for all of the snapshots of the trajectory. In the final step, an ensemble average of these ~10^7 scattering paths was generated and compared directly with the experimental spectra. This approach has led to a quantitative treatment of all photoelectron single and multiple scattering paths generating an EXAFS spectrum that captures all the structural details inherent in the MD simulation, including the bond lengths, bond angles, vibrational disorder, and local symmetry about the Al T-site.

Finally, the MD-EXAFS spectra (one for each of sets A, B, and C) based upon the DFT method are obtained. These spectra capture a high-level representation of the structure at the Al T-sites and are used as reference spectra to determine the Al T-site distribution in the HBEA150 and HBEA25 samples through linear combination fitting to the experimentally observed EXAFS, the fractional occupancies being the coefficients for the least-squares fit to the k-weighted $\chi(k)$ data.

XANES Calculations with Time-Dependent DFT. XANES calculations were performed at the Al K-edge for the T-sites considered in the NMR and EXAFS analysis using a TDDFT-based restricted excitation window as implemented in the NWChem quantum chemistry program.[55,56] This approach involves defining a model subspace of single excitations from the relevant core orbitals and is a valid ansatz because core excitation energies are well separated from pure valence−valence excitations.

For each Al T-site conformation, the Sapporo-QZP-2012[57] all-electron basis set was used for the single absorbing Al T-site and the nearest O atoms. The Si and O atoms further away were represented with the Stuttgart RLC ECPs.[58] The exchange-correlation was treated with the BHLYP functional.[59] All calculated spectra were Lorentzian-broadened by 1 eV and shifted by +16.8 eV to match the experimental spectrum.

DFT NMR Calculations. The NMR calculations (DFT NMR) for the HBEA Al T-sites were performed using the NWChem software package.[55] The T-sites were modeled in the dissociated state as $[Al-(O-Si-OH)_4]^-$ ions. The structures of the ions were derived from the DFT optimized crystal structures by cutting and terminating O−Si bonds with hydrogens while maintaining the bond directions. The O−H bond length was set to 0.96 Å in all cases. This size of cluster has been shown to be appropriate for zeolite ^{27}Al chemical shift calculations.[19] The cluster charge was set to "−1" to compensate for the dissociated Brønsted acidic proton. The

calculations used the B3LYP (Becke 3-parameter Lee−Yang−Parr exchange correlation functional).[59,60] The shielding property for a single Al^{3+} atom populating the DFT optimized HBEA unit cell was calculated using the 6-311+G** basis set[61] applied for the Al, O, Si, and H atoms. Note that the zeolite Si/Al ratio was shown to have no effect on the absolute MAS NMR peak shift values,[62] provided that there are no Al pairs (Al−O−Si-O−Al).[48] Thus, the DFT NMR can be calculated using identical structures for both HBEA150 and HBEA25. The NMR chemical shifts are referenced to aqueous Al^{3+} solution; however, the absolute chemical shielding tensor for this reference cannot be accurately determined by calculation because the disordered aqueous structure of the Al^{3+} standard solution is difficult to model. In the least-squares fitting procedure, the absolute chemical shift tensor for the reference was optimized, and the NMR line width and shape (Voigt function) for each T-site were assumed to be the same. This procedure provided an absolute chemical shielding tensor of 572.4 ppm for aqueous Al^{3+}. As a further point of reference, HMOR zeolite, which is chemically and structurally similar to HBEA, is calculated to have a chemical shift that is within 1 ppm of its measured value (see SI).

RESULTS AND DISCUSSION

Evaluation of α-Al_2O_3 and $Na_2Al_2O_4$ Crystalline Standards. In general, a comprehensive MD-EXAFS evaluation of the Al K-edge spectra has only rarely been used to evaluate the structure beyond the first Al−O shell. To demonstrate the sensitivity of EXAFS to the structure beyond the first Al−O shell, crystalline samples of α-Al_2O_3 and $Na_2Al_2O_4$ were evaluated in detail using the same MD-EXAFS methodology that is used to evaluate Al T-site distribution in the zeolites. Both of these compounds contain only one type of Al site. The analysis begins with their crystallographic structure,[63,64] which is the starting input for generating the MD trajectories. There are no adjustable parameters used to generate the respective MD-EXAFS spectrum that is then compared directly to the experimental one. The MD-EXAFS spectra for the two standards validate the method that is subsequently applied to the analysis of the more complex local structure of the $[Al-O_4]^-$ tetrahedra in the zeolite.

Figure 3a,b shows the $k^2\chi(k)$ plot for α-Al_2O_3 and the imaginary Fourier transform of this function in the form of the $Img[\tilde{\chi}(R)]$ plot. The MD-EXAFS calculation reproduces all the relevant features in $\chi(k)$, and it does an excellent job of reproducing the position and amplitudes of the peaks in the $Img[\tilde{\chi}(R)]$ over the full range from 1 to ~5 Å. It is worth noting that for α-Al_2O_3, there is a strong multielectron absorption edge at ~k = 5.3 Å^{-1} due to the $KL_{II,III}$ transition (Figure 3a). The amplitude of this multielectron edge represents ~50% of the amplitude of the EXAFS oscillations in this region. The Fourier transform of this feature may result in some high-frequency ripples in the $Img[\tilde{\chi}(R)]$ plots, although these ripples have a relatively minor effect on the distance and amplitude of the main spectral features. This multielectron edge appears to be much weaker for Al tetrahedral sites (e.g., zeolites). Preliminary delta self-consistent field (ΔSCF) calculations for α-Al_2O_3 and $Na_2Al_2O_4$ predict the multielectron edges at 115.81 and 115.86 eV from their respective K-edges. These are consistent with our experimental findings of 112.5 and 111.5 eV, respectively.

The same overall analysis procedure was applied to $Na_2Al_2O_4$, as shown in Figure 4. Again, all the relevant features
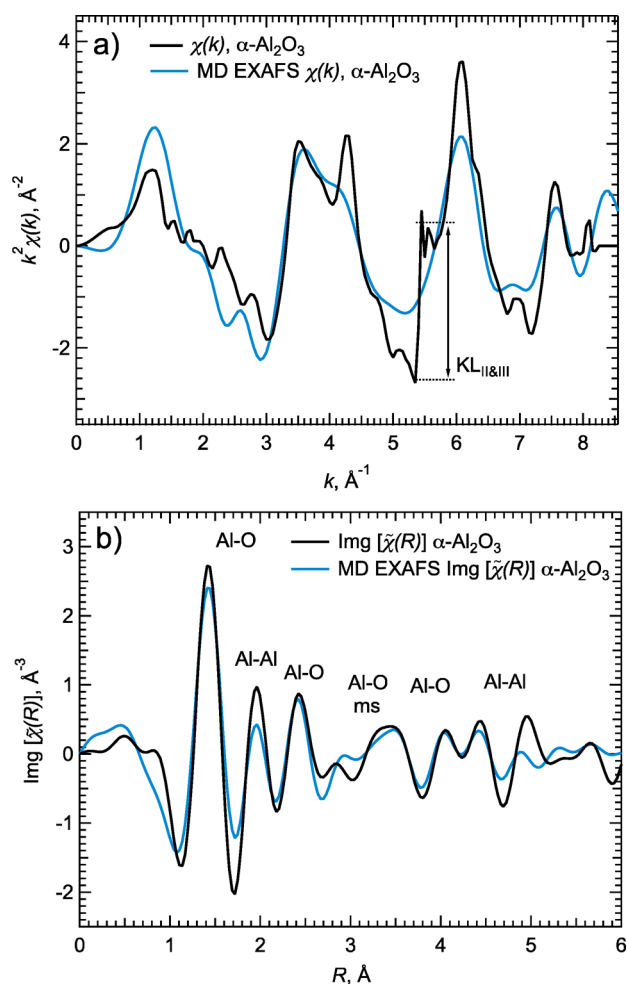
Figure 3. EXAFS k^2-weighted $\chi(k)$ (a) and Img[$\tilde{\chi}(R)$] (b) plots showing the experimental and MD-EXAFS calculated spectra of α-alumina.

Figure 4. EXAFS k^2-weighted $\chi(k)$ (a) and Img[$\tilde{\chi}(R)$] (b) plots showing the experimental and MD-EXAFS calculated spectra of $Na_2Al_2O_4$.

of both $\chi(k)$ and Img[$\tilde{\chi}(R)$] are captured by MD-EXAFS. There is a small phase mismatch in the Img[$\tilde{\chi}(R)$] plot in the region around 2.5−3 Å. Subsequent XRD analysis showed the existence of ~15% of the hydrate, $Na_4Al_4O_8 \cdot 5H_2O$, in the sample, and this may be the cause of the shifting of the Al−Al and Al−Na peaks to slightly longer distances in the experimental spectrum. Notably, the tetrahedrally coordinated $Na_2Al_2O_4$ shows only a small feature at the position of the $KL_{II,III}$ transition at $k = 5.3$ Å^{-1}.

The ability to successfully assign the features in the Img[$\tilde{\chi}(R)$] data from 1 to 5 Å establishes the distance-range sensitivity for both the experimental and simulated Al EXAFS measurements and provides justification to apply these methods to the characterization of the zeolite structure.

MD-EXAFS Evaluation of the Effect of the Brønsted Acidic Proton on the Al T-Site. In water-free HBEA zeolites, the negative charge at the Al T-site is balanced by a proton bonded to one of the bridging O atoms (Al−OH−Si). However, in the presence of adsorbed water, this proton exists as a hydronium ion (e.g., $(H_2O)_n \cdot H_3O^+$) that resides locally in the zeolite pore paired with the AlO_4^- T-site. Therefore, structures of protonated and unprotonated T-sites were calculated to determine how the structures differed and whether EXAFS could distinguish the differences. The DFT-optimized Al−O bond distances are summarized in Table 1 for
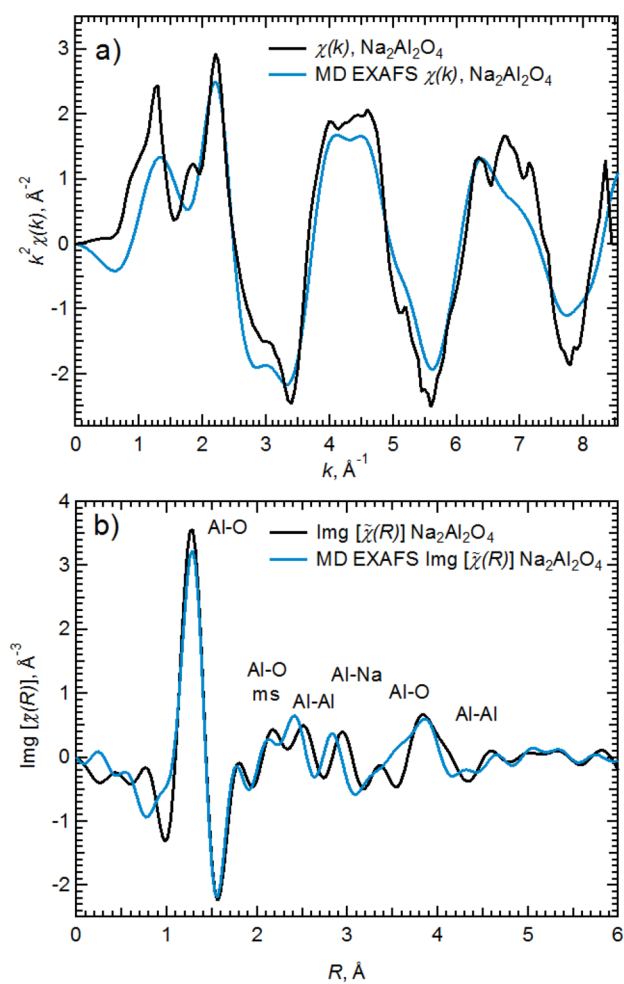
Table 1. Calculated Al−O Bond Distances (Å) for Unprotonated and Protonated Al T-Sites in HBEA Zeolite from Periodic DFT Optimized Structures^a

| T-site | unprotonated | protonated | |
	$O_3Al–O$	$(HO)O_2Al–O$	$O_3Al–OH$, Å
T1	1.74	1.70	1.92
T2	1.72	1.70	1.91
T3	1.73	1.71	1.87
T4	1.72	1.71	1.88
T5	1.72	1.70	1.89
T6	1.73	1.71	1.89
T7	1.74	1.70	1.96
T8	1.74	1.70	1.94
T9	1.73	1.69	1.94

^{a}The Al−O distances are averages of four values for the unprotonated site and three values for the protonated site, both averages having a standard deviation of 0.02 Å.

the nine T-sites in their protonated and unprotonated states (full list in SI). In general, the four first-shell Al−O bond distances are nearly identical in the unprotonated state. (It should be noted that this first-shell T-site similarity does not extend to the higher O and Si shell distances that provide the basis for discriminating the T-site occupancy by EXAFS).

When a proton is bonded to one of the bridging O atoms, that Al−O bond is elongated to ∼1.92 Å versus about 1.70 Å for the remaining three Al−O bonds. As shown in the analysis of α-Al_2O_3 and $Na_2Al_2O_4$, above, the EXAFS measurements have a spatial resolution of ∼0.15 Å (for k_{max} = 8 Å^{-1}). For this reason, it is possible to differentiate the protonated from the "unprotonated" state of the Al T-sites. This was firmly established by performing MD-EXAFS simulations on protonated and unprotonated T-sites.

Figure 5 shows the Img[$\tilde{\chi}(R)$] plots for the experimentally measured spectrum for HBEA150 and the simulated spectra of
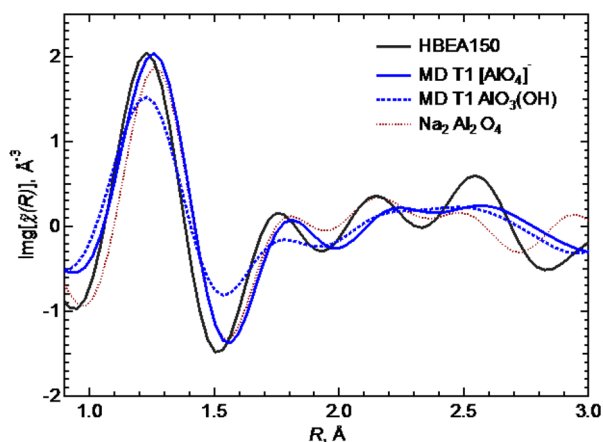

Figure 5. Img[$\tilde{\chi}(R)$] plot comparing the experimental HBEA150 spectrum (black) with the MD-EXAFS spectra for the T1 site in the [AlO_4]$^-$ (solid blue) and AlO_3(OH) (dashed blue) configurations and the experimental spectrum for $Na_2Al_2O_4$ (dashed red).

a protonated and unprotonated T-site. Because the first-shell Al−O distances are nearly the same in the nine different HBEA T-sites, only the T1 site is shown. For comparison, the EXAFS spectrum for tetrahedral $Na_2Al_2O_4$ is included. Figure 5 shows that the experimental spectrum for HBEA150 in the region between 1 and 1.75 Å is in quantitative agreement with the simulated value for the unprotonated site. The HBEA150 EXAFS spectrum is also seen to be similar to the tetrahedral $Na_2Al_2O_4$, in which the four Al−O bond lengths are equivalent. Although not shown, similar observations were made for HBEA25. Thus, it is concluded that for both HBEA150 and HBEA25, the T-sites are dissociated under measurement conditions, their negative charges being balanced by hydronium ions, and for this reason, subsequent analyses will be based on the T-site structures in the dissociated (unprotonated) state. Note that although the EXAFS measurements were made on the samples in vacuum, the ambient room temperature conditions were not sufficient to dehydrate hydronium ions.[65,66] The section that follows moves to a comprehensive analysis of the variation of longer-range Al−O and Al−Si distances at various T-sites beyond the first-shell Al−O distances.

Evaluating the Distribution of Al^{3+} among HBEA T-Sites from MD-EXAFS Analysis. HBEA zeolite contains nine different T-sites that could be populated with Al atoms. The distribution of Al−Si and Al−O distances (probed by EXAFS) within a given T-site can be correlated with the number of shared 4-, 5-, or 6-member rings (see Figure 1) at that T-site. On the basis of this premise, a DFT-based EXAFS spectrum was calculated for each of the nine T-sites, and it was found that they could be grouped into three sets—set A (T1, T2, T5, T6),

set B (T3, T4), and set C (T7, T8, T9)—by way of the similarity of their EXAFS spectra (see SI Figure 7S). Subsequently, full MD trajectories at 300 K were calculated for one representative T-site from each set (T1, T3, and T7 from sets A, B, and C, respectively), and these trajectories were, in turn, used to simulate the EXAFS spectra of the T-sites using the MD-EXAFS method. Figure 6 shows the full MD-EXAFS
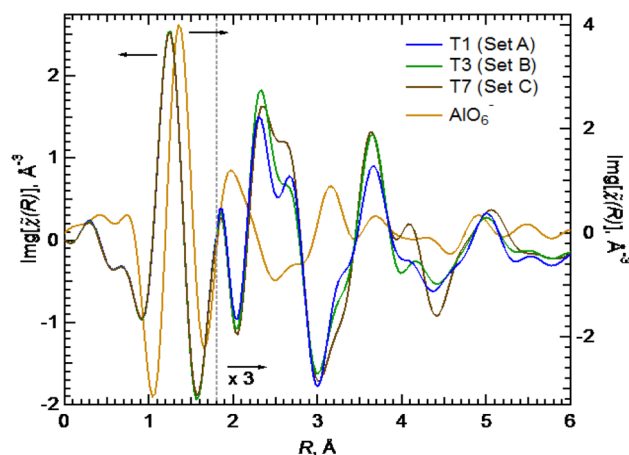

Figure 6. Img[$\tilde{\chi}(R)$] plots of the calculated MD-EXAFS spectra for sites T1 (blue), T3 (green), and T7 (brown) representing T-site sets A, B, and C, respectively. T1, T3, and T7 are rescaled beyond 1.8 Å, as shown, whereas the AlO_6^- spectrum is not. The AlO_6^- spectrum is from an experimentally measured aqueous Al^{3+}.

spectra generated for T-sites T1, T3, and T7. Note the significant spectral differences in the region from 2 < R < 5.5 Å owing to the different arrangements of Si and second-shell O atoms around the different Al T-sites. HBEA zeolites often contain small percentages of extra-framework AlO_6^- (octahedral) as an impurity. This species can be approximated by aqueous Al^{3+} that would have nearly the same first-shell Al−O bond distances and symmetry. The spectrum of aqueous Al^{3+} is shown in Figure 6 for comparison. The features for aqueous Al^{3+} are dominated by single and multiple scattering peaks (e.g., peak at 3.2 Å) from only the first-shell O's.

To provide an understanding of the structural similarities and differences between these sites and the groups they represent, the Al−Si and Al−O radial distribution functions, $g(r)$, generated from the MD trajectories of the three Al T-sites are compared in Figure 7. Both $g(r)_{Al-O}$ and $g(r)_{Al-Si}$ are shown because, although the EXAFS backscattering signal from O is not nearly as strong as for Si, the signal still contributes significantly to the total EXAFS spectra, and the contributions are distinct from those for Si. Peaks in the $g(r)$ plots at $g(r)_{Al-O}$ = 1.75 Å and $g(r)_{Al-Si}$ = 3.15 Å are due to the nearest-neighbor O and Si atoms about each Al. When the Al T-site is protonated, multiple peaks appear at these distances, as shown in Figure 7 for the Al T1-site (the dashed purple line). In the $g(r)_{Al-O}$ plot, two distinct peaks are seen. One intense peak for the three unprotonated oxygens bonded to Al appears at $g(r)_{Al-O}$ = 1.7 Å, and one of lower intensity for the protonated O appears at $g(r)_{Al-O}$ = 1.95 Å. In the $g(r)_{Al-Si}$ plot, two peaks appear at $g(r)_{Al-Si}$ = 3.1 and 3.25 Å, and a shoulder is evident at 3.45 Å. This analysis shows that the protonation state can be definitively determined from EXAFS measurements of the first-shell Al−O and Al−Si distances.
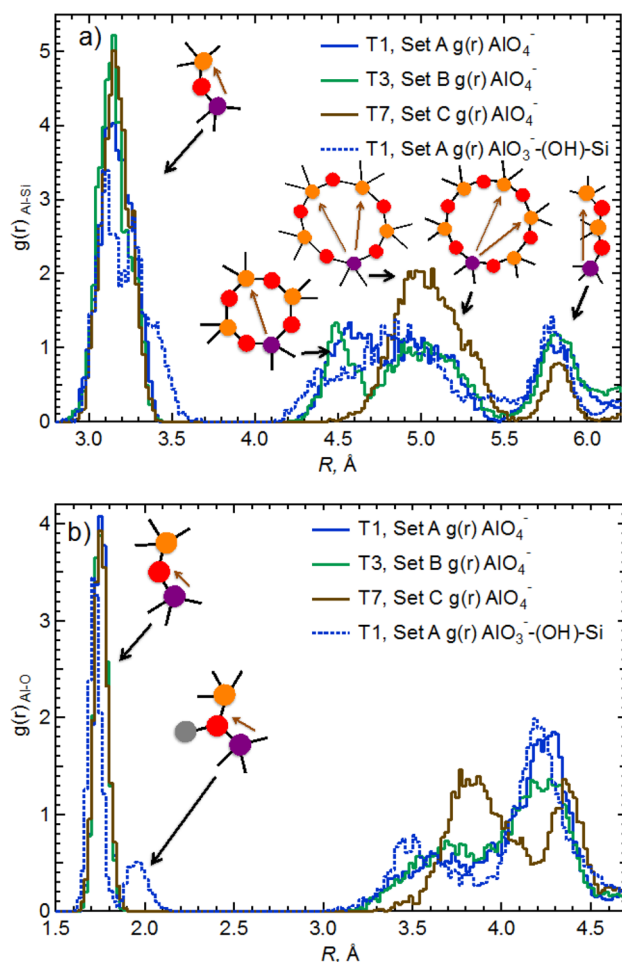
Figure 7. Calculated $g(r)$ plots for Al−Si (a) and Al−O (b) atom pairs; see legend for details. The corresponding unique structural features providing information about the framework are shown as schemes, Al (purple), O (red), Si (orange), H (gray) atoms. Note: pore structures are schematic, bond distances are not to scale.

EXAFS data may discriminate between the different structural sets. In addition, EXAFS multiple scattering signals depend upon the angular correlations of the nearby Si and O atoms, thereby further improving the structural resolution of bond lengths and symmetry. These multiple scattering features cannot be represented in the standard $g(r)$ plots, but they are quantitatively represented in the calculated MD-EXAFS spectra.

The measured HBEA150 and HBEA25 $\chi(k)$ data were fit as a linear combination of the full MD-EXAFS spectra (Figure 6 T-sites T1, T3 and T7) to determine the Al T-site occupancy of each zeolite. Since both zeolites contain small fractions of octahedrally coordinated Al present as extra-framework Al^{3+}, the measured spectrum of aqueous $Al(H_2O)_6^{3+}$ was used as a reference for octahedral Al (see SI). The presence of octahedral Al is clearly differentiated by both its unique EXAFS structure and by its near-zero chemical shift in NMR. Figure 8 shows the resulting analysis for the HBEA150 zeolite. The analysis for HBEA25 is shown in the Supporting Information. The T-site occupancies in HBEA150 and HBEA25 as determined by EXAFS (and by MAS NMR, as will be shown below) are shown
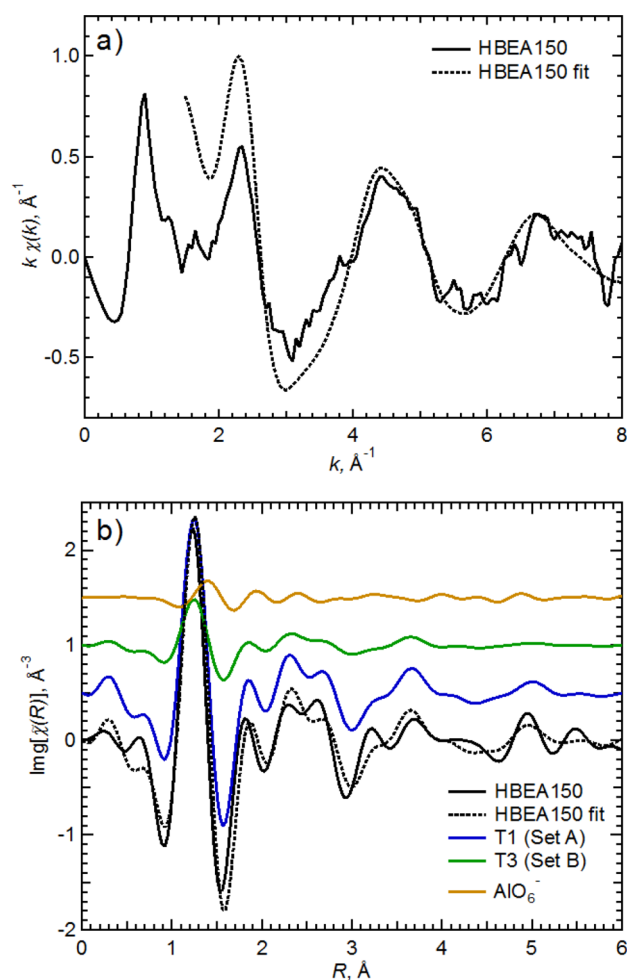
When the Al T-site is unprotonated (the expected experimental state), there is very little difference in the Al−O and Al−Si first-shell distances among the three different structural sets A, B, and C. Hence EXAFS cannot differentiate the structures solely upon the first-shell Al−O and Al−Si distances. In contrast, there are distinguishable differences in the second-shell Al−O and Al−Si distances. In sets A, B, and C, the Al T-sites share different combinations of 4-, 5-, and 6-member Al−O−(Si−O)$_{n-1}$ rings. The T-sites in sets A and B contain at least one 4-member ring. The second-shell Al−Si distances for these 4-member rings occur at a distance of 4.5 Å. Set C contains no 4-member rings, such that $g(r)_{Al-Si}$ shows a peak at a somewhat greater distance of ~5 Å for both 5- and 6-member rings. Although not nearly as distinct as for the 4-member rings, the atom distances for the 5-member rings are somewhat shorter than for 6-member rings. Analysis of the $g(r)_{Al-O}$ plot shows similar trends. The distributions of second-shell Al−O distances for sets A and B appear at shorter distances than for set C. All three structural sets of A, B, and C contain a component from a near linear arrangement of Al−O−Si−O-Si atoms leading to distinct peaks in the second-shell distances at $g(r)_{Al-O}$ = 4.2−4.4 Å and $g(r)_{Al-Si}$ = 5.8 Å. Thus, the differences in the distribution of Al−Si and Al−O distances revealed in the $g(r)$ plots provide an understanding of how the

Figure 8. EXAFS k-weighted $\chi(k)$ plots (a) for experimental HBEA150 and simulated using a linear combination of MD-EXAFS for T1 and T3 sites representing Al T-site sets A and B, respectively, and a measured aqueous $Al(H_2O)_6^{3+}$ EXAFS for octahedral Al; $Img[\tilde{\chi}(R)]$ plots (b) for experimental (solid black) and simulated (dotted black) HBEA150 with the calculated contributions for T-sites T1 (set A, blue), T3 (set B, green), and AlO_6^- (octahedral sites, gold).

in Table 2. It should again be emphasized that the three MD-EXAFS spectra (for set A, B, C) were generated from DFT

Table 2. Al T-Site Occupancies of HBEA150 and HBEA25 As Determined from EXAFS and NMR Spectra^a

HBEA150 EXAFS groups (T-sites)	occupancy^b		HBEA150 NMR T-sites (fraction)
	via EXAFS	via NMR	
set A (1, 2, 5, 6)	0.72	0.70	1 (0), 2 (0), 5 + 6 (0.70)
set B (3, 4)	0.19	0.24	3 (0.20), 4 (0.04)
set C (7, 8, 9)	0.0	0.0	7 (0), 8 (0), 9 (0)
AlO_6^- (octahedral)	0.09	0.06	AlO_6^- (octahedral)

HBEA25 EXAFS groups (T-sites)	occupancy^b		HBEA25 NMR T-sites (fraction)
	via EXAFS	via NMR	
set A (1, 2, 5, 6)	0.41	0.42	1 (0), 2 (0.33), 5 + 6 (0.09)
set B (3, 4)	0.0	0.0	3 (0), 4 (0)
set C (7, 8, 9)	0.38	0.35	7 (0.35), 8 (0), 9 (0)
AlO_6^- (octahedral)	0.21	0.23	AlO_6^- (octahedral)

^{a}The two zeolites vary not only in Al content but also in Al T-site distribution. Site occupancies are derived from fitting of experimental EXAFS and NMR spectra to their respective sets of theoretical standards. ^{b}The estimated errors are ±10% by EXAFS and ±10% by NMR.

methods without the need for any adjustable parameters. The percent occupancy was derived from fitting four spectra (three T-sites and one AlO_6^- site) using only three parameters representing the fractions of each component.

The results show that HBEA150 and HBEA25 have distinctly different distributions of Al T-sites. In the HBEA150, the sites are 70% populated by set A and 20% by set B, whereas in HBEA25, the sites are nearly equally populated by sets A and C. It is interesting that no sites of set C are present in HBEA150 and no sites of set B sites are in HBEA25. Neither Al distributions correlate well with that expected from the relative thermodynamic stability of the T-sites. The probabilities of Al to populate the nine unprotonated sites based on the degeneracies and the DFT energies are listed in SI Table 7S and graphically depicted in SI Figure 11S. Sites T7 and T8 are thermodynamically the most favored sites (probabilities of 0.87 and 0.12, respectively). Members of set C, both T7 and T8, are located in 6-member rings that are connected to the large 12-member ring in the [100] and [010] planes; however, these two sites never occur in the same 6-member ring. From the EXAFS analysis, ~50% of the tetrahedral Al in the measured HBEA25 may occupy site T7, but in HBEA150, none of the T7 sites appear to be occupied by Al. The EXAFS analysis shows that set A sites (T1, T2, T5, T6) in both HBEA150 and HBEA25 samples are occupied by Al to significant extents, although their thermodynamic probabilities of being occupied total less than 0.1%. The T3 and T4 sites (set B) have similarly low probabilities of being occupied, yet the EXAFS analysis shows that 20% of the tetrahedral Al in the HBEA150 sample is located in these sites. Therefore, the differences in Al^{3+} distributions from thermodynamic equilibrium suggest that the distributions are controlled by kinetic factors, which are unique to the methods in which the two zeolites were synthesized, and the dealumination procedure, which may lead to selective removal of Al from certain T-sites.

Evaluating the Occupancy of Al T-Sites from the NMR Analysis. The ^{27}Al MAS 900 MHz NMR spectra of HBEA 150 and HBEA25 are shown in Figure 9. The chemical shifts are in
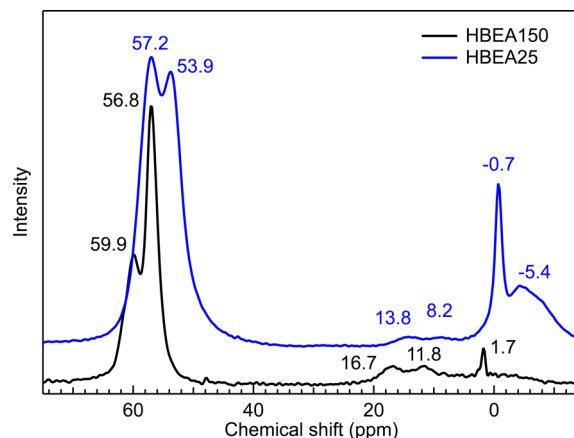

Figure 9. ^{27}Al MAS NMR spectra measured for HBEA150 (black) and HBEA25 (blue). The intensity of the HBEA25 spectrum was scaled (0.33) for better visualization.

agreement with chemical shift values previously reported for HBEA.[67,68] The peak positions and peak heights indicate that the zeolites have substantially different distributions of Al^{3+}. The peaks between −15 and 20 ppm are typical of extra-framework octahedral Al. From integration of the spectra, 23% of the Al in HBEA25 and 6% in HBEA150 occupy octahedral environments. These amounts are consistent with the EXAFS analysis (Table 2), which yielded 21 and 9%, respectively. The peaks between 50 and 65 ppm are attributed to tetrahedral Al in the zeolite framework. Although both zeolites exhibit a peak in this region at about 57 ppm, the 54 ppm signal present in HBEA25 is not observed in HBEA150, and the 60 ppm signal present in HBEA150 is not found in HBEA25. The presence of other Al species, for example, extra-framework tetrahedral Al, which would give rise to signals at ~30−45 ppm,[69,70] is excluded on the basis of the MAS NMR spectra. These findings are consistent with the EXAFS results, which showed that Al does not populate some T-sites.

DFT NMR calculations of ^{27}Al chemical shifts were performed to assign the T-sites that contribute to the observed peaks. The chemical shifts calculated for the nine different T-sites are compiled in SI Table 4S and shown graphically in Figure 10 on expanded plots of the NMR resonances for tetrahedral Al in the HBEA150 and HBEA25 samples. The calculated chemical shifts span from 53.9 to 62.5 ppm, which is significantly wider than the chemical shifts predicted using an empirical relationship based solely upon Al−O−Si bond angles (see SI Figure 9S).[11]

This suggests that the DFT NMR chemical shifts may be used to simulate the experimental spectra and, through a least-squares fitting procedure, determine the relative Al occupancy at each T-site. The fitting of DFT NMR shifts to the experimental ^{27}Al NMR spectra is performed completely independent of the EXAFS analysis and is not constrained in any way by the amounts of Al in the different T-site sets determined in the EXAFS analysis. To limit the number of parameters used in the fitting procedure, the NMR line width and shape (Voigt function) for each T-site were assumed to be identical. As shown in Figure 10a, the HBEA150 spectrum can
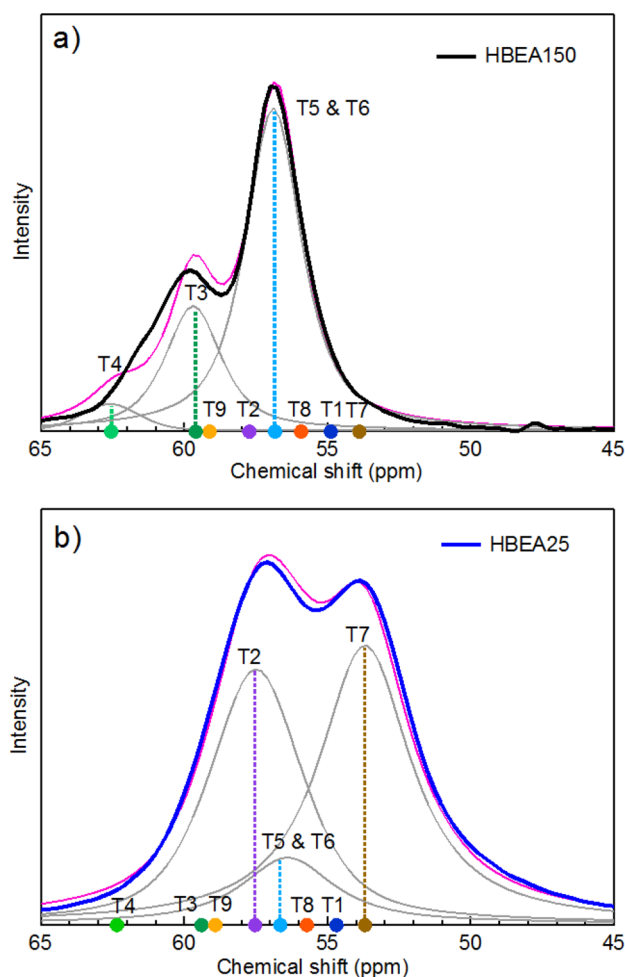
Figure 10. Calculated ^{27}Al MAS NMR chemical shifts for the tetrahedral Al based on the DFT optimized T-site structures for the measured HBEA150 (a) and HBEA25 (b). Fitted NMR peaks are shown in gray; the fit spectrum is shown in magenta. Note: the T5- and T6- signals overlap. DFT NMR peak intensity is based on fitting results.

be represented as a combination of three peaks assigned to T5 + T6 (coincident peaks) and T3 and T4. As shown in Figure 10b, the HBEA25 spectrum is best represented as a combination of T7, T2, and T5 + T6. The incorporation of additional peaks into the fitting procedure did not lead to an improvement in the DFT NMR fit to the experimental data. The Al T-site occupancies determined by fitting to the DFT NMR shifts are listed in Table 2, and for comparison, they are summed into the same sets of T-sites (A, B, C) that were defined by the MD-EXAFS analysis. The agreement with EXAFS on the distribution of Al among these sets of T-sites is excellent for both HBEA150 and HBEA25. Consistent with the observations from the EXAFS analysis, the Al^{3+} distribution in the HBEA25 (from NMR analysis) is found to be significantly different from the HBEA150.

Note that the NMR data then lead to a further refinement of the EXAFS-derived information with respect to the T-site occupancy. For HBEA150, the occupancy of T1 by Al can be excluded with high confidence because the calculated DFT NMR peak position is too far upfield to contribute significantly to the observed spectrum (see Figure 10a). For HBEA25, the Al occupancy of T1, T8, and T9 can be excluded for similar reasons. These refinements are reflected in the NMR

distributions reported in Table 2. Hence, the combination of EXAFS and NMR analysis allowed a more quantitative determination of the Al distribution among T-sites than either would have permitted alone.

Although not the primary focus of this study, the analysis provides new insight into the HBEA zeolite synthesis, thus demonstrating its potential to aid in understanding how synthesis methods affect Al distributions and ultimately to guide efforts to optimize catalytic efficiency. Both HBEA25 and HBEA150 are synthesized hydrothermally using templating agents. Note that HBEA150 was obtained from a parent zeolite (Si/Al ratio similar to that of HBEA25) that was dealuminated by steaming and leaching steps to achieve the high Si/Al ratio of 75. We speculate that the postprocessing steps cause selective removal of the T2 and T7 sites, whereas the T5 and T6 sites remain mostly intact. The description of the dealumination mechanism is incomplete at this point and requires a more comprehensive evaluation of the relation between zeolite synthesis methods and Al distribution.

Al XANES Analysis and TDDFT Al XANES Calculations. XANES spectra primarily represent core- to valence-state electronic transitions that, with the aid of theory, provide a sensitive probe of the bonding and structure in the vicinity of the target atom. Although a quantitative analysis of the XANES region is beyond the scope of this study, the TDDFT calculations of the near edge spectra qualitatively confirm the conclusions deduced from the combination of EXAFS and NMR methods. In Figure 11, XANES spectra for HBEA150 and HBEA25 are compared to their respective theoretical calculations using TDDFT theory.

Initially, the XANES spectra for the complete set of nine T-sites were calculated and compared. The findings (see Figure 13S in the SI) show that the XANES spectra for the T-sites can be grouped with high confidence into the same three sets (sets A, B, C) that are used for the EXAFS analysis. As a result, Figure 11 shows the spectra for sets A, B, and C that were obtained by averaging the XANES spectra for T-sites (T1, T2, T5, T6), (T3, T4), and (T7, T8, T9), respectively. Although there are significant differences in the spectral features of these three sets, they are insufficiently unique to determine the distribution of Al^{3+} at the same level as achieved by combining EXAFS and NMR data. For this reason, a representative spectrum was generated using the site occupancies derived from the EXAFS measurement. This linear combination of sets A, B, and C is shown Figure 11 (red lines). The linear combinations also include small contributions from octahedral Al (an experimental aqueous Al^{3+} spectrum is used to represent the octahedral Al fraction).

The XANES calculations lead to an assignment of the electronic transitions for the HBEA spectra in the range of ~1560 to ~1568 eV. The feature at ~1564.5 eV, which is prominent in set C but also present in sets A and B, is attributed to excitations from the Al 1s to a mixture of O 3p, Al 3p, and Al 3d states. The prominent feature at ~1567 eV is attributed to excitations from Al 1s to a mixture of O 3p, Al 3p states. The deviation from experiment beyond ~1568 eV is tentatively interpreted as multiple excitation effects, which are not included within the linear-response formulation of TDDFT and, hence, are not captured. Previous studies[56,71,72] have shown, however, that TDDFT calculations of XANES are very reliable up to ~10 eV from the rising edge, where single excitations are dominant. Overall, the linear combination of the TDDFT XANES spectra qualitatively predicts the features of
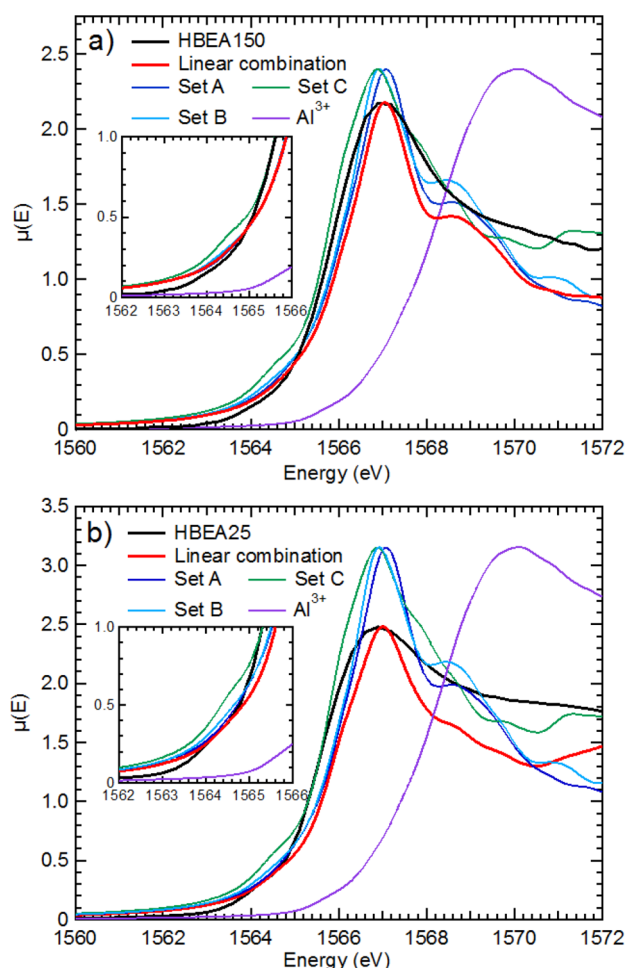
functioning as a template constituent. The distribution of Al T-sites in HBEA150 and HBEA25 differed markedly. Because the HBEA150 was prepared by leaching Al out of the lattice, we speculate that the lack of population in the T7- and the T2-sites, which are highly populated in HBEA25, is associated with the dealumination. It also points to the fact that T5 and T6 are resilient toward removal of Al. Although the details of this dealumination process are not explored at present, the analysis using a combination of EXAFS, NMR, and theory demonstrates the potential to analyze zeolite active sites in a depth and detail, which were not available hitherto.

■ ASSOCIATED CONTENT

ⓢ Supporting Information

HBEA XANES, XRD, and DFT optimized structures for HBEA T-sites as well as reference fitting parameters. This material is available free of charge via the Internet at http://pubs.acs.org.

■ AUTHOR INFORMATION

Corresponding Authors
E-mail: john.fulton@pnnl.gov
E-mail: johannes.lercher@pnnl.gov

Notes
The authors declare no competing financial interest.

■ ACKNOWLEDGMENTS

Figure 11. XANES $\mu(E)$ plots for the experimental HBEA150 (a) and HBEA25 (b). The EXAFS weighted linear combination of set A, set B, and octahedral Al (HBEA150) and set A, set C, and octahedral Al (HBEA25) are shown in red. The TDDFT calculated signals, set A (T1, T2, T5, T6) (dark blue), set B (T3, T4) (light blue), and set C (T7, T8, T9) (green), are also shown. The octahedral Al signal is shown in cyan. Note: the intensity of the measured Al^{3+} spectrum was scaled to the HBEA150 for comparison.

the experimental HBEA150 and HBEA25 spectra supporting the Al^{3+} distribution derived using the EXAFS and NMR spectroscopy methods.

■ CONCLUSION

An unprecedented level of structural detail regarding the distribution of Al^{3+} in the HBEA zeolite framework has been attained through a combination of X-ray absorption and NMR spectroscopies supported by ab initio computational models that enable quantitative analysis of the spectral data. The excellent quality of Al EXAFS allowed analysis of scattering from atoms up to 6 Å apart from the absorbing Al T-site and enabled the quantification of both framework and extra-framework Al^{3+}. The identical first-shell Al–O bond distances led us to conclude that hydronium ions are formed at all Al T-site to compensate the lattice charges. The population of T-sites with Al in HBEA150 and HBEA25 does not follow the population predicted by the thermodynamic stability of Al T-sites. This strongly suggests that the incorporation of Al into the zeolite lattice during hydrothermal synthesis is controlled by kinetics and primarily determined by the organic base

■ REFERENCES

(1) Feast, S.; Lercher, J. A. *Stud. Surf. Sci. Catal.* **1996**, *102*, 363.
(2) Lercher, J. A.; Jentys, A.; Brait, A. *Mol. Sieves Sci. Technol.* **2008**, *6*, 153.
(3) Davis, M. E. *Acc. Chem. Res.* **1993**, *26*, 111−115.
(4) Bhan, A.; Iglesia, E. *Acc. Chem. Res.* **2008**, *41*, 559−567.
(5) De Vos, D. E.; Dams, M.; Sels, B. F.; Jacobs, P. A. *Chem. Rev.* **2002**, *102*, 3615−3640.
(6) Gounder, R.; Iglesia, E. *J. Am. Chem. Soc.* **2009**, *131*, 1958−1971.
(7) Beyerlein, R. A.; Choi-Feng, C.; Hall, J. B.; Huggins, B. J.; Ray, G. J. *Top. Catal.* **1997**, *4*, 27−42.
(8) Sierka, M.; Eichler, U.; Datka, J.; Sauer, J. *J. Phys. Chem. B* **1998**, *102*, 6397−6404.
(9) Sauer, J.; Eichler, U.; Meier, U.; Schäfer, A.; von Arnim, M.; Ahlrichs, R. *Chem. Phys. Lett.* **1999**, *308*, 147−154.
(10) Katada, N.; Suzuki, K.; Noda, T.; Sastre, G.; Niwa, M. *J. Phys. Chem. C* **2009**, *113*, 19208−19217.
(11) Lippmaa, E.; Samoson, A.; Mägi, M. *J. Am. Chem. Soc.* **1986**, *108*, 1730.

8305

dx.doi.org/10.1021/ja501361v | *J. Am. Chem. Soc.* 2014, 136, 8296−8306

(12) van Bokhoven, J. A.; Koningsberger, D. C.; Kunkeler, P.; van Bekkum, H.; Kentgens, A. P. M. *J. Am. Chem. Soc.* **2000**, *122*, 12842.

(13) Kannelopoulos, J.; Unger, A.; Schwieger, W.; Freude, D. *J. Catal.* **2006**, *237*, 416−425.

(14) Dedecek, J.; Sobalik, Z.; Wichterlova, B. *Catal. Rev. Sci. Eng.* **2012**, *54*, 135−223.

(15) Kraus, H.; Prins, R.; Kentgens, A. P. M. *J. Phys. Chem.* **1996**, *100*, 16336.

(16) Sklenak, S.; Dedecek, J.; Li, C.; Wichterlova, B.; Gabova, V.; Sierka, M.; Sauer, J. *Phys. Chem. Chem. Phys.* **2009**, *11*, 1237−1247.

(17) Yu, Z.; Zheng, A.; Wang, Q.; Chen, L.; Xu, J.; Amoureux, J.-P.; Deng, F. *Angew. Chem., Int. Ed.* **2010**, *49*, 8657−8661.

(18) Dedecek, J.; Lucero, M. J.; Li, C.; Gao, F.; Klein, P.; Urbanova, M.; Tvaruzkova, Z.; Sazama, P.; Sklenak, S. *J. Phys. Chem. C* **2011**, *115*, 11056−11064.

(19) Sklenak, S.; Dedecek, J.; Li, C.; Wichterlova, B.; Gabova, V.; Sierka, M.; Sauer, J. *Angew. Chem., Int. Ed.* **2007**, *46*, 7286−7289.

(20) Sklenak, S.; Dedecek, J.; Li, C.; Wichterlova, B.; Gabova, V.; Sierka, M.; Sauer, J. *Phys. Chem. Chem. Phys.* **2009**, *11*, 1237−1247.

(21) Dedecek, J.; Sklenak, S.; Li, C.; Gao, F.; Brus, J.; Zhu, Q.; Tatsumi, T. *J. Phys. Chem. C* **2009**, *113*, 14454−14466.

(22) van Bokhoven, J. A.; Lee, T.-L.; Drakopoulos, M.; Lamberti, C.; Thieβ, S.; Zegenhagen, J. *Nat. Mater.* **2008**, *7*, 551.

(23) van Bokhoven, J. A.; Koningsberger, D. C.; Kunkeler, P.; van Bekkum, H. *J. Catal.* **2002**, *211*, 540−547.

(24) Manuel, D.; Cabaret, D.; Brouder, C.; Sainctavit, P.; Bordage, A.; Trcera, N. *Phys. Rev. B* **2012**, *85*, 224108.

(25) Drake, I. J.; Zhang, Y.; Gilles, M. K.; Liu, C. N. T.; Nachimuthu, P.; Perera, R. C. C.; Wakita, H.; Bell, A. T. *J. Phys. Chem. B* **2006**, *110*, 11665−11676.

(26) van Bokhoven, J. A.; van der Eerden, Ad M. J.; Prins, R. *J. Am. Chem. Soc.* **2004**, *126*, 4506−4507.

(27) Flank, A.-M.; Cauchon, G.; Lagarde, P.; Bac, S.; Janousch, M.; Wetter, R.; Dubuisson, J.-M.; Idir, M.; Langlois, F.; Moreno, T.; Vantelon, D. *Nucl. Instrum. Methods Phys. Res. B* **2006**, *246*, 269−274.

(28) Palmer, B. J.; Pfund, D. M.; Fulton, J. L. *J. Phys. Chem.* **1996**, *100*, 13393−13398.

(29) Amit, Y.; Eshet, H.; Faust, A.; Patllola, A.; Rabani, E.; Banin, U.; Frenkel, A. I. *J. Phys. Chem. C* **2013**, *117*, 13688−1369.

(30) Matsumoto, Y.; Murakami, M.; Shono, T.; Hasegawa, T.; Fukumura, T.; Kawasaki, M.; Ahmet, P.; Chikyow, T.; Koshihara, S.; Koinuma, H. *Science* **2001**, *291*, 854−856.

(31) Chica, A.; Corma, A. *J. Catal.* **1999**, *187*, 167−176.

(32) Rodriguez, I.; Climent, M. J.; Iborra, S.; Fornds, V.; Corma, A. *J. Catal.* **2000**, *192*, 441−447.

(33) Zhao, C.; Kou, Y.; Lemonidou, A. A.; Li, X.; Lercher, J. A. *Chem. Commun.* **2010**, *46*, 412−414.

(34) Zhao, C.; Camaioni, D. M.; Lercher, J. A. *J. Catal.* **2012**, *288*, 92−103.

(35) Corma, A.; Moliner, M.; Cantín, A.; Díaz-Cabañas, M. J.; Jordá, J. L.; Zhang, D.; Sun, J.; Jansson, K.; Hovmöller, S.; Zou, X. *Chem. Mater.* **2008**, *20*, 3218−3223.

(36) (a) Newsam, J. M.; Treacy, M. M. J.; Koetsier, W. T.; de Gruyter, C. B. *Proc. R. Soc. London A* **1988**, *420*, 375−405. (b) Treacy, M. M. J.; Newsam, J. M. *Nature* **1988**, *332*, 249−251.

(37) Willhammar, T.; Zhou, X. *Z. Kristallogr.* **2013**, *228*, 11−27.

(38) Andersen, A.; Govind, N.; Subramanian, L. *Mol. Simul.* **2008**, *34*, 1025−1039.

(39) Wright, P. A.; Zhou, W.; Perez-Pariente, J.; Arranz, M. *J. Am. Chem. Soc.* **2005**, *127*, 494−495.

(40) Fyfe, C. A.; Strobl, H.; Kokotailo, G. T.; Pasztor, C. T.; Barlow, G. E.; Bradley, S. *Zeolites* **1988**, *8*, 132−136.

(41) Cambior, M. A.; Corma, A.; Valencia, S. *Chem. Commun.* **1996**, 2365−2366.

(42) Martinez-Iñesta, M. M.; Peral, I.; Proffen, T.; Lobo, R. F. *Microporous Mesoporous Mater.* **2005**, *77*, 55−66.

(43) (a) Ravel, B.; Newville, M. *J. Synchrotron Radiat.* **2005**, *12*, 537. (b) Newville, M. *J. Synchrotron Radiat.* **2001**, *8*, 322.

(44) Fulton, J. L.; Balasubramanian, M. *J. Am. Chem. Soc.* **2010**, *132*, 12597−12604.

(45) Jiao, J.; Kanellopoulos, J.; Wang, W.; Ray, S. S.; Foerster, H.; Freude, D.; Hunger, M. *Phys. Chem. Chem. Phys.* **2005**, *7*, 3221−3226.

(46) (a) The CP2K Developers Group. *CP2K Open Source Molecular Dynamics Program*; http://www.CP2K.org/; accessed May 2014. (b) VandeVondele, J.; Krack, M.; Mohamed, F.; Parrinello, M.; Chassaing, T.; Hutter, J. *Comput. Phys. Commun.* **2005**, *167*, 103.

(47) International Zeolite Association. *Framework Structure Database*; http://izasc-mirror.la.asu.edu/fmi/xsl/IZA-SC/ft.xsl, accessed May 2014.

(48) Dedecek, J.; Sklenak, S.; Li, C.; Wichterlova, B.; Gabova, V.; Brus, J.; Sierka, M.; Sauer, J. *J. Phys. Chem. C* **2009**, *113*, 1447−1458.

(49) Goedecker, S.; Teter, M.; Hutter, J. *Phys. Rev. B* **1996**, *54*, 1703.

(50) VandeVondele, J.; Hutter, J. *J. Chem. Phys.* **2007**, *127*, 114105.

(51) Perdew, J. P.; Burke, K.; Ernzerhof, M. *Phys. Rev. Lett.* **1996**, *77*, 3865.

(52) Higgins, J. B.; LaPierre, R. B.; Schlenker, J. L.; Rohrman, A. C.; Wood, J. D.; Kerr, G. T.; Rohrbaugh, W. J. *Zeolites* **1988**, *8*, 446−452.

(53) VandeVondele, J.; Rothlisberger, U. *J. Phys. Chem. B* **2002**, *106*, 203.

(54) Fulton, J. L.; Bylaska, E. J.; Bogatko, S.; Balasubramanian, M.; Cauët, E.; Schenter, G. K.; Weare, J. H. *J. Phys. Chem. Lett.* **2012**, *3*, 2588.

(55) Valiev, M.; Bylaska, E. J.; Govind, N.; Kowalski, K.; Straatsma, T. P.; Van Dam, H. J. J.; Wang, D.; Nieplocha, J.; Apra, E.; Windus, T. L.; de Jong, W. A. *Comput. Phys. Commun.* **2010**, *181*, 1477.

(56) Lopata, K.; Van Kuiken, B. E.; Khalil, M.; Govind, N. *J. Chem. Theory Comput.* **2012**, *8*, 3284.

(57) Noro, T.; Sekiya, M.; Koga, T. *Theoret. Chem. Acc.* **2012**, *131*, 1124.

(58) Schuchardt, K. L.; Didier, B. T.; Elsethagen, T.; Sun, L.; Gurumoorthi, V.; Chase, J.; Li, J.; Windus, T. L. *J. Chem. Inf. Model.* **2007**, *47* (3), 1045−1052.

(59) Becke, A. D. *J. Chem. Phys.* **1993**, *98*, 1372−1377.

(60) Lee, C.; Yang, W.; Parr, R. G. *Phys. Rev. B* **1988**, *37*, 785.

(61) McLean, A. D.; Chandler, G. S. *J. Chem. Phys.* **1980**, *72*, 5639−5648.

(62) Han, O. H.; Kim, C.-S.; Hong, S. B. *Angew. Chem., Int. Ed.* **2002**, *41*, 469−472.

(63) Lewis, J.; Schwarzenbach, D.; Flack, H. D. *Acta Crystallogr. A* **1982**, *38*, 733.

(64) Kaduk, J. A.; Pei, S. *J. Solid State Chem.* **1995**, *115*, 126−139.

(65) Huang, J.; Jiang, Y.; Marthala, V. R. R.; Thomas, B.; Romanov, E.; Hunger, M. *J. Phys. Chem. C* **2008**, *112*, 3811−3818.

(66) Jiang, Y.; Huang, J.; Dai, W.; Hunger, M. *Solid State Nucl. Magn. Res.* **2011**, *39*, 116−141.

(67) van Bokhoven, J. A.; van der Berden, A. M. J.; Koningsberger, D. C. *J. Am. Chem. Soc.* **2003**, *125*, 7435−7442.

(68) Maier, S. M.; Jentys, A.; A Lercher, J. *J. Phys. Chem. C* **2011**, *115*, 8005−8011.

(69) Deng, F.; Yue, Y.; Ye, C. *J. Phys. Chem. B* **1998**, *102*, 5252−5256.

(70) Hunger, M.; Engelhardt, G.; Weitkamp, J. *Microporous Mater.* **1995**, *3*, 497.

(71) Van Kuiken, B. E.; Valiev, M.; Daifuku, S. L.; Bannan, C.; Strader, M. L.; Cho, H.; Huse, N.; Schoenlein, R. W.; Govind, N.; Khalil, M. *J. Phys. Chem. A* **2013**, *117*, 4444.

(72) Zhang, Y.; Biggs, J. D.; Healion, D.; Govind, N.; Mukamel, S. *J. Chem. Phys.* **2012**, *137*, 194306.